



Combining nitrogen substitutional defects and oxygen intercalation to control the graphene corrugation and doping level



Ana Martín-Recio ^{a,1}, Carlos Romero-Muñiz ^{b,1}, Pablo Pou ^{b,c}, Rubén Pérez ^{b,c,*},
José M. Gómez-Rodríguez ^{a,c,d,**}

^a Departamento de Física de la Materia Condensada, Universidad Autónoma de Madrid, E-28049, Madrid, Spain

^b Departamento de Física Teórica de la Materia Condensada, Universidad Autónoma de Madrid, E-28049, Madrid, Spain

^c Condensed Matter Physics Center (IFIMAC), Universidad Autónoma de Madrid, E-28049, Madrid, Spain

^d Instituto Nicolás Cabrera, Universidad Autónoma de Madrid, E-28049, Madrid, Spain

ARTICLE INFO

Article history:

Received 21 November 2017

Received in revised form

18 December 2017

Accepted 29 December 2017

Available online 3 January 2018

Keywords:

Graphene

Nitrogen doping

Scanning tunneling microscopy

Density functional theory

ABSTRACT

By means of Scanning Tunneling Microscopy (STM) experiments and first-principles calculations, we demonstrate the synergetic effect of the combination of two different strategies to modify the properties of graphene supported on a strongly interacting substrate like Rh. A complete control of the corrugation and doping level is achieved combining the introduction of nitrogen defects and oxygen intercalation. Firstly, we show how to use ion bombardment to obtain purely-substitutional N-doped graphene on Rh(111) with tunable dopant concentration. In a second step, the interaction with the substrate is controlled by the amount of intercalated oxygen atoms. Unlike weakly interacting substrates, the highly corrugated structure of G/Rh(111) leads to remarkable variations of the electronic properties associated with nitrogen defects created in the high and low areas of the moiré. After oxygen intercalation, the N-doped graphene layer decouples from the substrate preserving the incorporated nitrogen atoms, which display a subtle dependence of the STM contrast. First-principles calculations confirm the identification of substitutional N-defects and the recovery of the Dirac cone with a tunable shift governed by the nitrogen concentration. Our results support the combination of different modification techniques to tailor structural and electronic properties of graphene and other 2D materials.

© 2018 Elsevier Ltd. All rights reserved.

1. Introduction

Ten years after the isolation of graphene [1] we are still pursuing the way of implementing it as an active element in the next technology revolution [2]. In order to take advantage of the outstanding properties of graphene [3–6], and related 2D materials [7], in potential applications, such as electronic devices [8,9], catalysis [10–12] or membrane technology [13,14], we must be capable of tuning the structural and electronic properties of these materials according to the requirements of each specific task. The necessary modifications of the electronic properties include the control of

charge carrier concentration or mobility, the opening of a band gap or the shift of the Dirac cone towards *p* or *n* regions.

Graphene applications also require the production of large areas with a low defect concentration. The close-packed surfaces of transition metals have proved to be an excellent substrate for graphene growth by Chemical Vapor Deposition (CVD) [15,16]. Additionally, these substrates offer a way to tune the graphene properties exploiting the strength of the graphene–metal coupling [17,18], from the strongly interacting cases of Rh(111) [19], Re(0001) [20] or Ru(0001) [21,22] –leading to a highly corrugated graphene with a strong hybridization with the substrate that totally destroys the Dirac cone–, to the quasi-free-standing graphene grown in Pt(111) [23,24], Pt₃Ni(111) [25], Ag(111) [26] or Cu(111) [27,28], and intermediate cases like Ir(111) [29,30] or Pd(111) [31,32] with crossover properties.

Apart from the selection of the most appropriate substrate, alternative modification strategies include the deposition on top of the graphene of different molecules [33,34] or nanoclusters [35],

* Corresponding author. Departamento de Física Teórica de la Materia Condensada, Universidad Autónoma de Madrid, E-28049, Madrid, Spain.

** Corresponding author. Departamento de Física de la Materia Condensada, Universidad Autónoma de Madrid, E-28049, Madrid, Spain.

E-mail addresses: ruben.perez@uam.es (R. Pérez), josem.gomez@uam.es (J.M. Gómez-Rodríguez).

¹ These authors contributed equally to this work.

the intercalation of atomic [36] or molecular (especially water) species [36–38] in the confined interface between the graphene layer and the metallic substrate, and the introduction of heteroatoms, such as nitrogen [39] or boron [40], in the graphene lattice. The latter approach serves a double goal. The inclusion of substitutional defects with a different number of valence electrons leads to a net doping of the graphene layer either positive, for boron, or negative, in the case of nitrogen, shifting the Dirac cone accordingly [41]. On the other hand, these defects clearly enhance the chemical reactivity of the initially inert graphene, making it an interesting platform for multiple chemical reactions [39], especially those of oxygen reduction [42,43], and opening the door for its application as an efficient biosensor [44].

However, the production of purely substitutional N-graphene is a challenge. Initial attempts by a CVD process—similar to the one used for graphene but with an additional precursor like ammonia [42,43,45,46] or organic heterocycles [47–49] as nitrogen source—led to a poor control of the dopant concentration and a multitude of different nitrogen defects [42,43,47,49]. This issue is especially relevant because different types of defects give opposite contributions to the doping [50], leading to a final cancelation of the overall doping. Even after a careful selection of the underneath substrate, the N-doped graphene produced by CVD still contains a too wide variety of defects [51].

Here, we overcome this problem using low energy ion bombardment to obtain purely substitutional N-doped graphene supported on Rh(111) with a controlled dopant concentration, that can be tuned through the exposure time and the energy of the ions during bombardment. Our method, based on previous proposals to incorporate heteroatoms in graphene through ion bombardment [52–55], achieves on a highly reactive metal as Rh the same excellent results in terms of homogeneity and defect variability already shown on graphite [55], graphene grown on SiC(0001) [56] and weakly interacting metals like Pt(111) [57]. N substitutionals on different areas of the highly corrugated G/Rh(111) moiré lead to a markedly different STM contrast but first-principles simulations allow us to establish the nature of these defects. Furthermore, we have combined N doping with oxygen intercalation on this G/Rh(111) system. After the sequential application of these two processes, the N-doped graphene layer becomes flat and the electronic properties of pristine graphene are restored, with a shift in the Dirac cone that can be tuned by the opposite doping induced by the N substitutional defects and the interaction with the O/Rh substrate. The power of mixing doping and intercalation revealed by our results suggest that other combined schemes involving different modification techniques could dramatically improve our ability to tailor the properties of graphene and other 2D materials.

2. Methods

2.1. Experiments

All the experiments and sample preparations in this work were carried out under ultra-high vacuum (UHV) conditions with a base pressure of 1×10^{-10} Torr. The UHV system is equipped with a homemade variable temperature scanning tunneling microscope (VT-STM) [58,59] and a four-grid LEED/Auger optics. All steps of sample preparation were checked by LEED measurements and STM analysis. All STM data were measured and processed (including the theoretical images) with the WSxM software [60].

Graphene growth. The (111) surface of a high purity Rh single crystal was cleaned by several sputtering-annealing cycles: argon sputtering at room temperature (1 keV, 20 min) followed by a 15 min annealing at 950 °C in an oxygen atmosphere ($P_{\text{oxygen}} = 2 \times 10^{-7}$ Torr) to avoid carbide formation at the surface

from carbon segregation from the bulk. After, graphene growth was carried out via low pressure chemical vapor deposition (UHV-CVD) of ethylene at 850 °C ($P_{\text{ethylene}} = 2 \times 10^{-7}$ Torr). As a result, the sample was completely covered by a monolayer of high quality graphene.

Nitrogen doping. After graphene growth, nitrogen implantation was performed by means of 10 min low energy (100 eV) ion bombardment (mostly N_2^+). It was carried out using the same ion gun used for cleaning purposes ($P_{\text{N}_2} = 2.8 \times 10^{-7}$ Torr, impact angle 45°). Then, the sample was annealed at 840 °C for 10 min with the purpose of reconstructing the graphene layer from possible defects created during the bombardment. Following this procedure, more than 90% of the defects are substitutional nitrogen atoms as determined by comparing a large number of STM images with DFT calculations. Further details of this method can be found in Ref. [57].

Oxygen intercalation was carried out on doped samples by exposing them to 6×10^{-7} Torr of high purity oxygen gas. In order to activate this process, the sample was kept at 270 °C. A careful control of the temperature is mandatory to avoid graphene oxidation. With these conditions 80 min of oxygen exposure was required to complete the intercalation process in this system. This final state can be confirmed by LEED patterns where the typical $2 \times 2/2 \times 1$ periodicity from the oxygen atoms arrangement at the interface is achieved.

2.2. Computational details

We used Density Functional Theory (DFT) as implemented in the VASP code [61] with a plane-wave basis set defined by a cutoff of 400 eV together with projector augmented wave (PAW) pseudo-potentials [62,63] for all species involved (carbon, nitrogen, oxygen and rhodium). The Generalized Gradient Approximation (GGA) functional proposed by Perdew, Burke and Ernzerhof (PBE) [64] was used to describe the electronic exchange and correlation interactions. This functional was supplemented with the D2 semi-empirical correction [65] to take into account dispersion forces. We have checked that spin-polarization is not required in any of the studied systems.

We determined the equilibrium lattice parameter for bulk rhodium (3.7729 Å) and for graphene (2.4678 Å). Thanks to the expertise gained in previous work [19,66] we are able to construct unit cells with periodic boundary conditions of different experimentally observed moiré patterns of the G/Rh(111) system. In this work most of the calculations are performed on a rhombic unit cell whose side length is 16.17 Å corresponding to a graphene reconstruction of $[(\sqrt{43} \times \sqrt{43})\text{-R}7.6^\circ]_{\text{G}}$ on top of a four-layer rhodium slab with $(6 \times 6)_{\text{Rh}}$ cell. This unit cell contains a total of 230 atoms (86 carbon atoms and 144 rhodium atoms) which serves as starting point to analyze different experimental systems. By substituting one carbon atom by a nitrogen atom in different locations we are able to reproduce the experimental conditions for the N-doped graphene grown on Rh(111) with a fixed dopant concentration of N/C at. = 1.16%. By introducing 16 extra oxygen atoms located on alternate FCC-hollow positions we can reproduce the fully intercalated G/O-(2×1)/Rh(111) system. Finally we can substitute again one carbon atom by a dopant in this new configuration to reproduce the N-doped graphene on the O-(2×1)/Rh(111). Additionally, a larger cell constituted by two identical cells arranged along the x axis was used to study the effects of dopant concentration (see Supporting information for further details).

All structures were subjected to ionic relaxations following a conjugate gradient algorithm until forces upon atoms were less than 0.01 eV/Å. During these relaxations, the two bottom layers of the slab were kept fixed in their bulk positions while the rest of the

atoms, including the intercalated oxygens, were allowed to relax. The reciprocal space was sampled using a $2 \times 2 \times 1$ Monkhorst-Pack grid [67] during ionic relaxations and, then, it was increased until $9 \times 9 \times 1$ in single-point calculations to explore electronic properties, where a gaussian smearing of $\sigma = 0.1$ eV has been used. Finally theoretical STM images were obtained from the local density of states of the different cells according to the Tersoff-Hamann formalism [68,69].

3. Results and discussion

3.1. N-doped graphene on Rh(111)

We studied the substitutional nitrogen defects introduced on the G/Rh(111) surface by ionic implantation on a sample in which graphene fully covers the Rh(111) surface. Graphene was grown using the CVD process discussed in the previous section. Graphene on Rh(111) adopts different rotational domains [19] but it shows a clear preference for a single periodicity constituted by a $(12 \times 12)_G$ reconstruction aligned with a $(11 \times 11)_{Rh}$ cell of Rh(111). The resulting graphene layer is highly corrugated, with distinct low and high areas where G–Rh distances vary from 1.94 Å to 3.15 Å [19]. As a result, the unit cell of the moiré pattern, depicted in the inset of Fig. 1a, displays clearly distinguishable motifs with ternary symmetry corresponding to areas with different adsorption distances. In STM images, this structure is viewed as a combination of dark and bright triangular-shaped areas.

After ion implantation and subsequent annealing, large areas of N-doped graphene supported on Rh(111), like those presented in Fig. 1a, were obtained. Nitrogen atoms can be indistinctly incorporated either in the high or the low areas of the moiré pattern. In each case, the contrast around the heteroatom observed in STM experiments is clearly different. Nitrogen atoms located on high areas (Fig. 1b) are visualized as a dark feature inside bright

triangular spots, whose internal structure resembles the typical STM fingerprint of substitutional nitrogen atoms in weakly interacting systems [56,70] or graphite [71]. On the other hand, for atoms incorporated in the lowest areas (Fig. 1c), the achievement of atomic resolution is much more difficult. However, it is still possible to identify some barely visible distortions, associated with the defects, that appear as a dark feature with brighter surroundings. These results show how the STM fingerprint of nitrogen defects in the G/Rh system is distorted by the modulations of the rippled structure of graphene. Although the atomic position of the nitrogen atom always appears as a dark spot, the contrast of the surrounding carbon atoms, which is clearly influenced by the degree of hybridization with the substrate, is markedly different. Since the curvature of the lowest areas is larger, the distortion is also more evident, affecting even the ternary symmetry of the fingerprint, and precluding a straightforward identification of these defects as N substitutionals.

DFT calculations allow us to confirm the nature of the N defects and provide detailed information about their atomic structure and electronic properties. As pointed out in the methods section, we have performed these calculations with the VASP code [61] using a plane-wave basis set and the PBE exchange–correlation functional [64] supplemented by the D2 semi-empirical approach [65] to account for dispersion forces. In this section, all calculations are performed on a rhombic unit cell (with side length of 16.17 Å) that corresponds to a graphene reconstruction of $[(\sqrt{43} \times \sqrt{43})-R7.6^\circ]_G$ on top of a four-layer rhodium slab with a $(6 \times 6)_{Rh}$ cell. This experimentally observed moiré [19] shares the main features of the most common moiré pattern of $(12 \times 12)_G$, and, being smaller, helps to reduce the cost of the DFT simulations. By substituting one carbon atom by a nitrogen atom in different locations of this unit cell we are able to reproduce the experimental conditions for the N-doped graphene grown on Rh(111) with a fixed dopant concentration of N/C atoms = 1.16%.

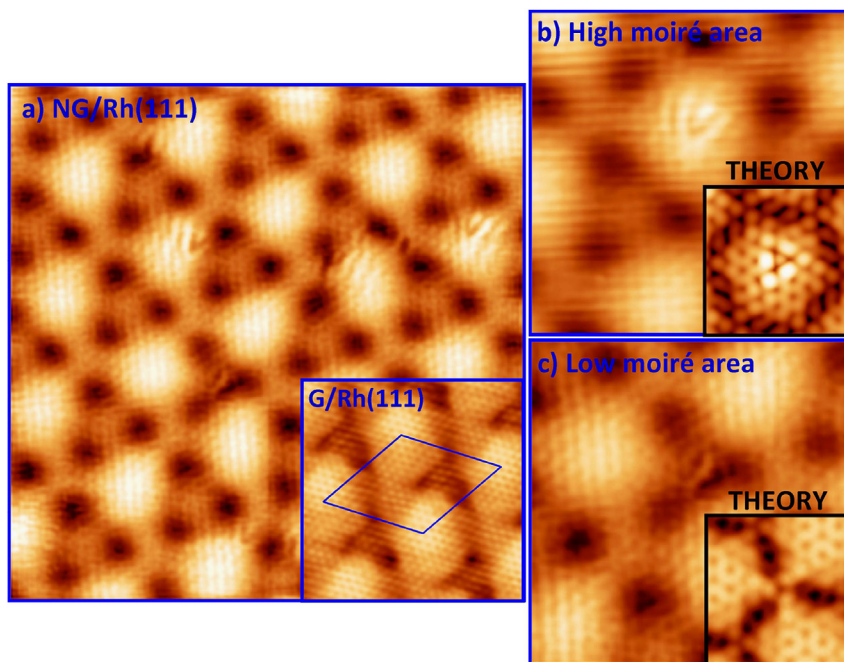


Fig. 1. (a) STM image of large areas ($12 \times 12 \text{ nm}^2$) of graphene grown on Rh(111) with some substitutional nitrogen defects incorporated on both the high and low areas of the moiré pattern ($I_t = 9.8 \text{ nA}$, $V_s = 0.47 \text{ V}$). In the inset ($6 \times 6 \text{ nm}^2$) the original G/Rh(111) interface before nitrogen implantation is shown ($I_t = 2.0 \text{ nA}$, $V_s = 0.45 \text{ V}$). The moiré pattern unit cell of 29.5 Å is also depicted with blue solid lines. (b) and (c) Magnified areas of the sample ($5 \times 5 \text{ nm}^2$) showing in more detail the nitrogen defects in the high ($I_t = 9.8 \text{ nA}$, $V_s = 0.56 \text{ V}$) (b) and low ($I_t = 9.8 \text{ nA}$, $V_s = 0.47 \text{ V}$) (c) areas of the moiré pattern. Each of them is accompanied by a theoretical image ($2 \times 2 \text{ nm}^2$) calculated with the Tersoff-Hamann formalism at the same voltages. The values used for the charge density isosurface are 1×10^{-5} au, and 6×10^{-7} au, respectively.

Theoretical STM images obtained with the Tersoff-Hamann formalism [68,69] for an N substitutional in the high and low areas of the moiré are shown in the corresponding insets of Fig. 1b and c. The results of these calculations are in good agreement with their experimental counterparts. This concordance allows us to unequivocally identify the observed STM features in both the high and low areas as substitutional nitrogen defects. Therefore, combining theory and experiment, we conclude that over 90% of defects appearing on the samples are substitutional nitrogen atoms, demonstrating the efficiency of the ion bombardment production method also in highly coupled graphene-metal systems.

In order to characterize the nature of the nitrogen dopants in this system and to understand the different STM contrast, we analyzed in detail the electronic structure of these defects. Fig. 2 shows the projected density of states (PDOS) of the nitrogen atom (N) and other four relevant carbon atoms (C1, C2, C3 and C4) in the surroundings of defects belonging to different regions of the moiré pattern. In each case the selected atoms are highlighted by circles of different colors in the insets.

In the high areas (Fig. 2a), the PDOS of the nitrogen atom clearly dominates over the surrounding carbon atoms despite appearing dark in STM experiments. This dark appearance, in spite of the large PDOS, has been extensively discussed on the recent literature [56,70–72] and it is attributed to the higher confinement of N wave functions in the normal direction, compared to the more extended states of the surrounding C atoms. More importantly, the N atom selectively donates charge to the surrounding carbon atoms and changes their STM contrast. This doping is very local and confined to carbon atoms in the opposite sublattice to the one where the N atom is located: The extra charge introduced by the dopant spreads mainly to the closest neighbors belonging to the opposite sublattice like C1 and C3. This enhancement of the PDOS is evident when

comparing the magenta and red solid curves of Fig. 2a with the dashed lines corresponding to the same atoms in the absence of nitrogen. On the contrary, no changes are induced in the carbon atoms in the sublattice of the defect (C2) or C atoms further away (C4), where the PDOS remains very similar to the undoped case. This behavior is similar to the one found in the N-doped G/Pt(111) interface. The local enhancement on the PDOS around the defect is responsible for the typical STM fingerprint of substitutional nitrogen atoms, with its characteristic six-point triangular shape with a dark center, previously reported for Pt(111) [57] or Cu(111) [70,73]. Notice that, in the G/Rh system, the large corrugation induced by strong interaction between the graphene layer and the substrate –with non-negligible differences in the G-Rh distance among neighboring atoms–, causes some distortion on this ideal fingerprint.

On the other hand, the situation on the low areas, presented in Fig. 2b, seems to be quite different. Although there is also an increment in the PDOS of the nitrogen defect and the nearest carbon atoms with respect to the undoped case, this enhancement of the PDOS is confined just to the first carbon neighbors in the opposite sublattice and spreads over a wider energy range. This can be clearly seen in the changes induced in the PDOS of atoms C1 and C3, that are equivalent by the three-fold symmetry to those shown in Fig. 2a. Similarly to the high area case, the effect of the dopant on atoms belonging to the sublattice of the defect (like C2) or located further away (C4) are minimal. The strong spatial localization of the doping and the fact that the associated changes in the PDOS are not confined to states close to the Fermi level but spread over a wide energy range can be attributed to the higher degree of hybridization of the carbon atoms in the low areas with the substrate. These two effects are responsible for the much weaker STM contrast associated with the same N substitutional defects when they are

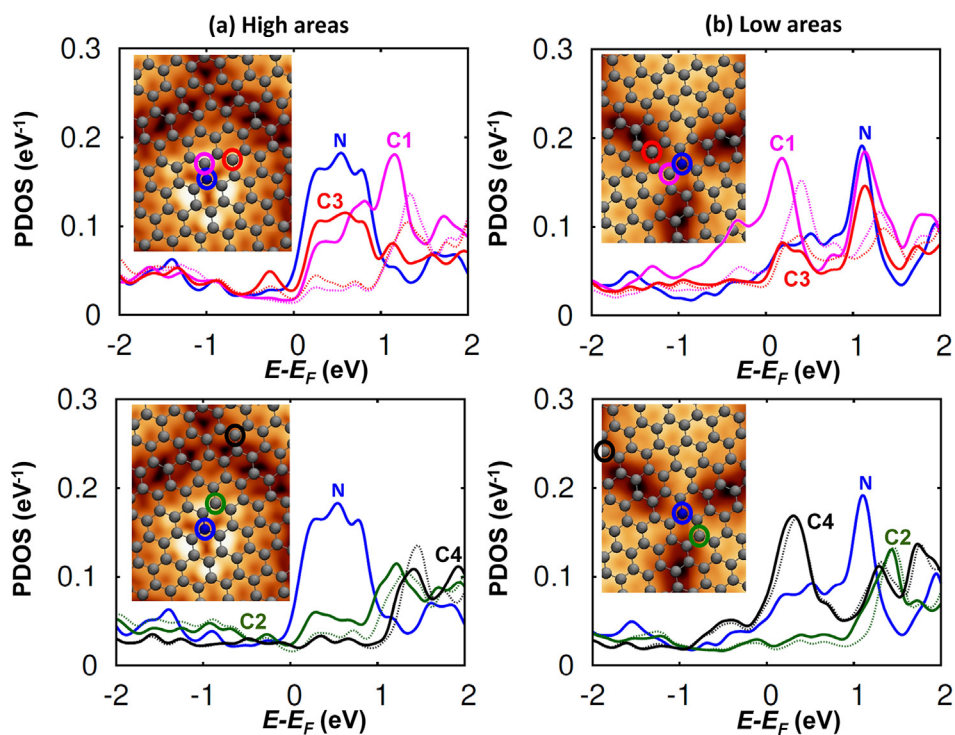


Fig. 2. Projected density of states (PDOS) of N-doped graphene for substitutional defects in high (a) and low (b) areas of the moiré pattern of G/Rh(111). In both cases the nitrogen atom (N) and some representative carbon atoms are selected to show their electronic properties (solid lines), C1, C2 and C3 are first, second and third neighbors respectively and C4 is a far neighbor. Dashed lines correspond to the equivalent carbon atoms in the free-nitrogen system. These atoms are highlighted with circles of different colors in the corresponding theoretical STM images (displayed as insets) where the graphene lattice has been superimposed. The bias voltages for this theoretical STM are (a) $V_s = +0.56$ V and (b) $V_s = +0.47$ V.

located in the low areas, making them barely visible and even affecting the ternary symmetry of their fingerprints.

In summary, the combination of STM experiments and first principles calculations allows us to confirm that low energy ionic implantation and subsequent annealing can be used to introduce substitutional nitrogen defects also in graphene supported on a strongly interacting metal like Rh(111). In the resulting highly corrugated moiré, we must distinguish between defects located on different areas according to the adsorption distance and the hybridization degree. While the influence of nitrogen doping is essentially the same in both the high and low areas of the moiré, the corrugation of the graphene layer, which modulates the degree of coupling with the substrate, produces relevant changes on the electronic properties and the STM appearance of the nitrogen defects.

3.2. N-doped graphene on O/Rh(111)

Although graphene electronic properties and chemical reactivity could be enhanced by nitrogen doping, there are still many capabilities which are not accessible by solely using this modification technique. For example, the *n*-like shift attributed to substitutional nitrogen defects is not observable in a strongly interacting system as G/Rh(111) due to the absence of a well-defined Dirac cone. Additionally, the high corrugation displayed by graphene in this substrate cannot be altered by the incorporation of N defects, and a greater flatness might be required for some applications. For this reason, we have explored the possibility of achieving a better control of different graphene properties following a novel strategy: to exploit the synergy between different modification techniques. In particular, we use nitrogen doping and subsequent oxygen intercalation to illustrate this idea.

Oxygen (and other metallic atoms) intercalation has proved to be an excellent option for tuning properties like graphene corrugation or the coupling with the substrate that cannot be tailored via N-doping. It has been successfully carried out in different undoped graphene-metal systems like Ru(0001) [74,75], Ir(111) [76], Ni(111) [77,78] or Rh(111) [66]. The ultimate intention is always to decouple epitaxial graphene from metal substrates restoring the electronic properties of a pristine graphene layer. In particular, in the G/Rh(111) interface, oxygen intercalation ends when a O-(2 × 1) network has been formed at the interface. According to DFT calculations, the final corrugation of graphene is 11 pm and the Dirac cone is restored and shifted to +0.63 eV [66].

Our proposal to improve our control of graphene properties is precisely to intercalate oxygen atoms in the confined space between the N-doped graphene layer and the Rh substrate. The success of this process will not only lead to a control of the G-metal coupling—and hence, the corrugation—that is governed by the amount of intercalated oxygen at the interface, but to the fine tuning of the graphene doping, that results from the combination of the *p*-contribution coming from the interaction with the O/Rh substrate and the amount of *n*-doping provided by the N-substitutionals, that can be controlled by the defect concentration.

This process has been implemented using the same approach already applied to undoped G/Rh(111) [66], and full oxygen intercalation, with the formation of a O-(2 × 1) monolayer on top of the Rh(111) surface has been achieved in the doped case. Fig. 3a–d shows different STM images of the same area of N-doped graphene after oxygen intercalation. These images, taken at different bias voltages, reveal a marked dependence of the contrast on the surroundings of the nitrogen atoms with bias: the fingerprint associated with the same defect under the same tunneling conditions changes with the applied bias voltage. For high positive bias (e.g. Fig. 3d), the characteristic bright triangular feature associated with

substitutional nitrogen defects is clearly observed. This supports our identification of those defects, confirming that they have not been affected by the intercalation process. Conversely, at low bias (Fig. 3a–b), this feature disappears giving rise to an STM contrast dominated by a dark spot, corresponding to the atomic position of the nitrogen defect, surrounded also by dark areas of carbon atoms that extend around ~15 Å and are independent of the moiré modulations.

The explanation for this peculiar behavior can be elucidated after analyzing the structure and the electronic properties of this system extracted from our DFT calculations. Similarly to the undoped case, the G layer becomes fully detached from the substrate, displaying the same average adsorption distance, 3.93 Å, and a slightly smaller corrugation, 8 pm (vs. 11 pm for the undoped case). This reduction is due to the compressive strain field induced by the shortening of the C–N bonds with respect to the original C–C bonds. The Tersoff-Hamann STM images associated with this structure display the same characteristics of the experimental images: the triangular fingerprint at high bias voltages (Fig. 3i), which disappears at lower bias voltages, as shown in Fig. 3h. The good agreement between these calculations and their experimental counterparts (see Fig. 3e and 3h) allows us to further confirm that substitutional nitrogen atoms remain after the intercalation process, assessing the reliability of the experimental procedure.

The evolution of the STM contrast of the nitrogen defect with the applied bias can be understood in terms of the calculated PDOS. Fig. 3f shows the PDOS of the nitrogen atom (N) and three representative carbon atoms (C1, C2 and C3 in the inset of Fig. 3f). The most prominent feature of this electronic structure is the total recovery of a Dirac cone, located 0.45 eV above the Fermi level, which was completely absent before intercalation. This effect is more evident in the carbon atoms in the defect sublattice (C2) and those far from the defect (C3) where the PDOS shows a clearly symmetric Dirac cone. The electronic structure at the right side of the Dirac cone resembles very much the one found in other weakly interacting systems [56,57]. The PDOS of the nitrogen atom is remarkably larger compared to carbon atoms, with a clear enhancement of the PDOS on the closer C atoms in the sublattice opposite to the defect, that is responsible for the bright triangular feature at large bias. Conversely, at the left side of the Dirac cone, the situation inverts. The PDOS of carbon atoms far from the defect (e.g. C3) starts to grow over the PDOS of the nitrogen atom and its nearest neighbors. This asymmetry found in the electronic structure is responsible for the marked dependence of the STM contrast with respect to the bias voltage.

Another important feature revealed by DFT calculations is that this system is very sensitive to variations on defect concentration. To study the influence of the dopant concentration we have used two simulation cells with different sizes. The DFT results shown in Fig. 3 correspond to a unit cell whose size is twice the one used in the previous section, that is a (12 × 6)_G. This unit cell is constructed by joining two (6 × 6)_G cells along the *x* axis, doubling the length of the corresponding Bravais vectors to 32.34 Å. Since both cells contain a single nitrogen atom the concentrations are N/C at. = 1.16% and N/C at. = 0.58%. The main change in the electronic structure is the larger shift in the Dirac point towards the *p*-region, moving away from the Fermi level, for smaller dopant concentrations (see Fig. S1 in Supporting Information). This change, together with the smaller PDOS of N atoms on the left side of the Dirac cone, also affects to the STM contrast of nitrogen defects (see Fig. S2 in Supporting Information). Note that the experimental defect concentration (N/C at. ≈ 0.1%), far lower than the values used in our calculations, are not achievable on standard computational resources. As a result, the Dirac point in the PDOS on Fig. 3f (+0.45 eV) is slightly displaced with respect to the experimental value, that

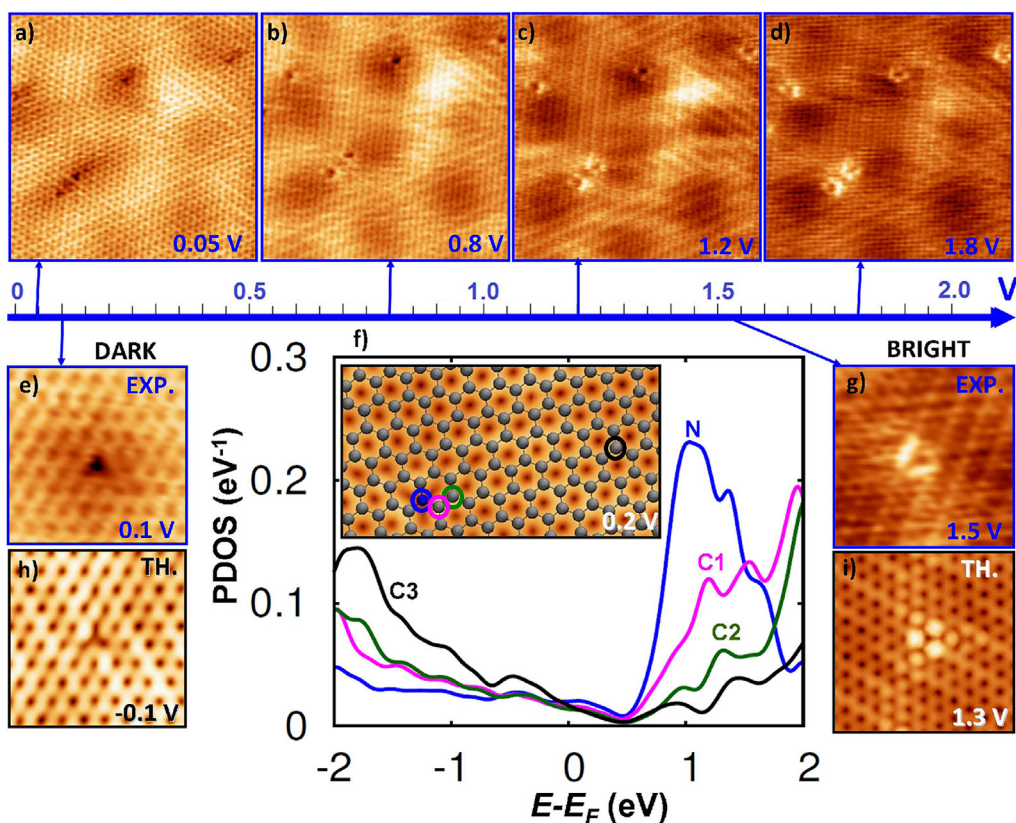


Fig. 3. Substitutional nitrogen defects on G/Rh(111)-O(2×1) after oxygen intercalation. (a–d) A set of STM images ($8 \times 8 \text{ nm}^2$) containing several nitrogen defects at the same tunneling current conditions ($I_t = 4.0 \text{ nA}$) and with different bias voltages indicated in blue. The images show the progressive change in the contrast of nitrogen defects from dark for low positive voltages to bright for voltages larger than 1 V. STM images (e) and (g) are magnified areas of a single defect ($2 \times 2 \text{ nm}^2$, $I_t = 4.0 \text{ nA}$, $V_s = 0.1 \text{ V}$) and ($2.5 \times 2.5 \text{ nm}^2$, $I_t = 6.7 \text{ nA}$, $V_s = 1.5 \text{ V}$). Images (h) and (i) are the corresponding theoretical counterparts of the single-defect images calculated with the Tersoff-Hamann approximation with a shift of 0.2 eV in the voltage (see text for explanation). The values of the isosurface are $1 \times 10^{-7} \text{ au.}$ and $5 \times 10^{-7} \text{ au.}$ In (f), the projected DOS of the nitrogen atom (N) and the three carbon atoms (C1, C2 and C3) highlighted in the inset are plotted. Notice the strong asymmetry between the two sides of the Dirac cone in the PDOS for the N and the closer carbon atoms C1 and C2 with respect to more distant carbon atoms like C3.

is very close to the position of the Dirac point for a system with no nitrogen defects and the same oxygen coverage at the interface (+0.63 eV) [66]. Thus, a rigid shift of roughly $\sim 0.2 \text{ V}$ must be considered when comparing theoretical and experimental results (see the STM images of Fig. 3e and 3h, and Fig. 3g and 3i). Considering this shift, there is a good agreement with the experimental results. The only experimental feature that is not reproduced by the theoretical calculations is the large dark area around the N defects for low bias voltages. This is also a direct consequence of the higher concentration used in simulations (see Fig. S2 in Supporting Information). Thus, once the influence of the defect concentration is taken into account, our calculations unambiguously prove that the electronic properties of the carbon atoms near the nitrogen defects—in particular, the asymmetry of the PDOS around the Dirac point—are responsible for the changes in the STM appearance of these defects with the bias voltage.

4. Conclusions

In this work, we have demonstrated the synergetic effect of combining two different strategies to modify the graphene properties, nitrogen defects and oxygen intercalation, in order to achieve a complete control of the corrugation and doping level of graphene supported on a strongly interacting metal like Rh.

Firstly, we have extended the protocol used on weakly-interacting substrates, based on low energy ion implantation and high-temperature annealing, to introduce purely substitutional

nitrogen defects with a tunable concentration in the G/Rh(111) system. With the variable incorporation of nitrogen defects, we introduce an additional *n*-like contribution to the graphene layer apart from the substrate doping. The STM features associated with N atoms in the high and low areas of the highly corrugated G/Rh(111) moiré are markedly different, but DFT calculations provide an explanation for the contrast and confirm the identification as N substitutionals.

Subsequently, the intercalation of oxygen atoms at the N-doped graphene–metal interface allow us to control the degree of coupling with the substrate and the corrugation of the layer, from a highly rippled configuration with a strong substrate hybridization to a completely uncoupled and flat layer for the 2×1 oxygen saturation coverage. After completing the intercalation process, STM images confirm the presence of a homogeneous collection of nitrogen substitutionals with associated patterns that change significantly with the applied bias voltage. DFT calculations support this identification, explain the bias dependence on the asymmetry with respect to the Dirac point of the PDOS of the N and the neighboring carbon atoms, and reveal the strong dependence of the electronic properties on the N concentration, showing that the final doping level can be fine tuned by the opposite effect of the *p* contribution coming from the O/Rh(111) substrate and the *n*-doping provided by the N substitutional defects.

Our results confirm the advantages of combining different modification techniques in order to tailor simultaneously structural and electronic properties of graphene. We expect that similar

combined routes for graphene modification based on several independent techniques will contribute to control the functionality of graphene and other 2D materials in the search of a better performance or completely novel applications.

Acknowledgement

We thank the financial support from AEI and FEDER under project MAT2016-77852-C2-2-R (AEI/FEDER, UE) and from MINECO under projects CSD2010-00024, MAT2014-54484-P and MDM-2014-0377. Computer time provided by the Spanish Supercomputer Network (RES) at the Magerit (CesViMa, Madrid) supercomputer. CRM is grateful to FPI-UAM graduate scholarship program and Fundación Universia for financial support.

Appendix A. Supplementary data

Supplementary data related to this article can be found at <https://doi.org/10.1016/j.carbon.2017.12.117>.

References

- [1] K.S. Novoselov, A.K. Geim, S.V. Morozov, D. Jiang, Y. Zhang, S.V. Dubonos, I.V. Grigorieva, A.A. Firsov, *Science* 306 (2004) 666.
- [2] A.C. Ferrari, F. Bonaccorso, V. Fal'ko, K.S. Novoselov, S. Roche, P. Boggild, S. Borini, F.H.L. Koppens, V. Palermo, N. Pugno, J.A. Garrido, R. Sordan, A. Bianco, L. Ballerini, M. Prato, E. Lidorikis, J. Kivioja, C. Marinelli, T. Ryhanen, A. Morpurgo, J.N. Coleman, V. Nicolosi, L. Colombo, A. Fert, M. Garcia-Hernandez, A. Bachtold, G.F. Schneider, F. Guinea, C. Dekker, M. Barbone, Z. Sun, C. Galiotis, A.N. Grigorenko, G. Konstantatos, A. Kis, M. Katsnelson, L. Vandersypen, A. Loiseau, V. Morandi, D. Neumaier, E. Treossi, V. Pellegrini, M. Polini, A. Tredicucci, G.M. Williams, B. Hee Hong, J.-H. Ahn, J. Min Kim, H. Zirath, B.J. van Wees, H. van der Zant, L. Occhipinti, A. Di Matteo, I.A. Kinloch, T. Seyller, E. Quesnel, X. Feng, K. Teo, N. Rupesinghe, P. Hakonen, S.R.T. Neil, Q. Tannock, T. Lofwander, J. Kinaret, *Nanoscale* 7 (2015) 4598.
- [3] A.H. Castro Neto, F. Guinea, N.M.R. Peres, K.S. Novoselov, A.K. Geim, *Rev. Mod. Phys.* 81 (2009) 109.
- [4] A.A. Balandin, S. Ghosh, W. Bao, I. Calizo, D. Teweldebrhan, F. Miao, C.N. Lau, *Nano Lett.* 8 (2008) 902.
- [5] C. Lee, X. Wei, J.W. Kysar, J. Hone, *Science* 321 (2008) 385.
- [6] F. Bonaccorso, Z. Sun, T. Hasan, A.C. Ferrari, *Nat. Photon* 4 (2010) 611.
- [7] A. Gupta, T. Sakthivel, S. Seal, *Prog. Mater. Sci.* 73 (2015) 44.
- [8] F. Schwierz, *Nat. Nanotechnol.* 5 (2010) 487.
- [9] G. Fiori, F. Bonaccorso, G. Iannaccone, T. Palacios, D. Neumaier, A. Seabaugh, S.K. Banerjee, L. Colombo, *Nat. Nanotechnol.* 9 (2014) 768.
- [10] C. Huang, C. Li, G. Shi, *Energy Environ. Sci.* 5 (2012) 8848.
- [11] X. Fan, G. Zhang, F. Zhang, *Chem. Soc. Rev.* 44 (2015) 3023.
- [12] D. Deng, K.S. Novoselov, Q. Fu, N. Zheng, Z. Tian, X. Bao, *Nat. Nanotechnol.* 11 (2016) 218.
- [13] S. Gadipelli, Z.X. Guo, *Prog. Mater. Sci.* 69 (2015) 1.
- [14] A. Gugliuzza, A. Politano, E. Drioli, *Curr. Opin. Chem. Eng.* 16 (2017) 78.
- [15] X. Li, W. Cai, J. An, S. Kim, J. Nah, D. Yang, R. Piner, A. Velamakanni, I. Jung, E. Tutuc, S.K. Banerjee, L. Colombo, R.S. Ruoff, *Science* 324 (2009) 1312.
- [16] A. Reina, X. Jia, J. Ho, D. Nezich, H. Son, V. Bulovic, M.S. Dresselhaus, J. Kong, *Nano Lett.* 9 (2009) 30.
- [17] M. Batzill, *Surf. Sci. Rep.* 67 (2012) 83.
- [18] H. Tetlow, J.P. de Boer, I.J. Ford, D.D. Vvedensky, J. Coraux, L. Kantorovich, *Phys. Rep.* 542 (2014) 195.
- [19] A. Martín-Recio, C. Romero-Muñiz, A.J. Martínez-Galera, P. Pou, R. Pérez, J.M. Gómez-Rodríguez, *Nanoscale* 7 (2015) 11300.
- [20] E. Miniussi, M. Pozzo, A. Baraldi, E. Vesselli, R.R. Zhan, G. Comelli, T.O. Menteş, M.A. Niño, A. Locatelli, S. Lizzit, D. Alfè, *Phys. Rev. Lett.* 106 (2011), 216101.
- [21] P.W. Sutter, J.-I. Flege, E.A. Sutter, *Nat. Mater.* 7 (2008) 406.
- [22] A.L. Vázquez de Parga, F. Calleja, B. Borca, M.C.G. Passeggi, J.J. Hinarejos, F. Guinea, R. Miranda, *Phys. Rev. Lett.* 100 (2008), 056807.
- [23] M.M. Ugeda, D. Fernández-Torre, I. Brihuega, P. Pou, A.J. Martínez-Galera, R. Pérez, J.M. Gómez-Rodríguez, *Phys. Rev. Lett.* 107 (2011), 116803.
- [24] M. Gao, Y. Pan, L. Huang, H. Hu, L.Z. Zhang, H.M. Guo, S.X. Du, H.-J. Gao, *Appl. Phys. Lett.* 98 (2011), 033101.
- [25] A. Politano, G. Chiarello, *2D Mater.* 4 (2017), 035003.
- [26] B. Kiraly, E.V. Iski, A.J. Mannix, B.L. Fisher, M.C. Hersam, N.P. Guisinger, *Nat. Commun.* 4 (2013) 2804.
- [27] L. Gao, J.R. Guest, N.P. Guisinger, *Nano Lett.* 10 (2010) 3512.
- [28] A.J. Martínez-Galera, I. Brihuega, J.M. Gómez-Rodríguez, *Nano Lett.* 11 (2011) 3576.
- [29] J. Coraux, A.T. N'Diaye, C. Busse, T. Michely, *Nano Lett.* 8 (2008) 565.
- [30] A.T. N'Diaye, J. Coraux, T.N. Plasa, C. Busse, T. Michely, *N. J. Phys.* 10 (2008), 043033.
- [31] S.-Y. Kwon, C.V. Ciobanu, V. Petrova, V.B. Shenoy, J. Bareño, V. Gambin, I. Petrov, S. Kodambaka, *Nano Lett.* 9 (2009) 3985.
- [32] Y. Murata, E. Starodub, B.B. Kappes, C.V. Ciobanu, N.C. Bartelt, K.F. McCarty, S. Kodambaka, *Appl. Phys. Lett.* 97 (2010), 143114.
- [33] J.M. MacLeod, F. Rosei, *Small* 10 (2014) 1038.
- [34] G. Li, L. Huang, W. Xu, Y. Que, Y. Zhang, J. Lu, S. Du, Y. Liu, H.-J. Gao, *Phil. Trans. R. Soc. A* 372 (2014), 20130015.
- [35] X. Liu, Y. Han, J.W. Evans, A.K. Engstfeld, R.J. Behm, M.C. Tringides, M. Hupalo, H.-Q. Lin, L. Huang, K.-M. Ho, D. Appy, P.A. Thiel, C.-Z. Wang, *Prog. Surf. Sci.* 90 (2015) 397.
- [36] Q. Fu, X. Bao, *Chem. Soc. Rev.* 46 (2017) 1842.
- [37] X. Feng, S. Maier, M. Salmeron, *J. Am. Chem. Soc.* 134 (2012) 5662.
- [38] A. Politano, M. Cattelan, D.W. Boukhvalov, D. Campi, A. Cupolillo, S. Agnoli, N.G. Apostol, P. Lacovig, S. Lizzit, D. Farías, G. Chiarello, G. Granozzi, R. Larciprete, *ACS Nano* 10 (2016) 4543.
- [39] H. Wang, T. Maiyalagan, X. Wang, *ACS Catal.* 2 (2012) 781.
- [40] S. Agnoli, M. Favaro, *J. Mater. Chem. A* 4 (2016) 5002.
- [41] X. Wang, G. Shi, *Phys. Chem. Chem. Phys.* 17 (2015) 28484.
- [42] L. Qu, Y. Liu, J.-B. Baek, L. Dai, *ACS Nano* 4 (2010) 1321.
- [43] D. Geng, Y. Chen, Y. Chen, Y. Li, R. Li, X. Sun, S. Ye, S. Knights, *Energy Environ. Sci.* 4 (2011) 760.
- [44] Y. Wang, Y. Shao, D.W. Matson, J. Li, Y. Lin, *ACS Nano* 4 (2010) 1790.
- [45] X. Wang, X. Li, L. Zhang, Y. Yoon, P.K. Weber, H. Wang, J. Guo, H. Dai, *Science* 324 (2009) 768.
- [46] D. Wei, Y. Liu, Y. Wang, H. Zhang, L. Huang, G. Yu, *Nano Lett.* 9 (2009) 1752.
- [47] D. Usachov, O. Vilkov, A. Grüneis, D. Haberer, A. Fedorov, V.K. Adamchuk, A.B. Preobrajenski, P. Dudin, A. Barinov, M. Oehzelt, C. Laubschat, D.V. Vyalyikh, *Nano Lett.* 11 (2011) 5401.
- [48] Z. Jin, J. Yao, C. Kittrell, J.M. Tour, *ACS Nano* 5 (2011) 4112.
- [49] Y.-F. Lu, S.-T. Lo, J.-C. Lin, W. Zhang, J.-Y. Lu, F.-H. Liu, C.-M. Tseng, Y.-H. Lee, C.-T. Liang, L.-J. Li, *ACS Nano* 7 (2013) 6522.
- [50] T. Schiros, D. Nordlund, L. Pálková, D. Prezzi, L. Zhao, K.S. Kim, U. Wurstbauer, C. Gutiérrez, D. Delongchamp, C. Jaye, D. Fischer, H. Ogasawara, L.G.M. Pettersson, D.R. Reichman, P. Kim, M.S. Hybertsen, A.N. Paspupathy, *Nano Lett.* 12 (2012) 4025.
- [51] D. Usachov, A. Fedorov, O. Vilkov, B. Senkovskiy, V.K. Adamchuk, L.V. Yashina, A.A. Volykhov, M. Farjam, N.I. Verbitskiy, A. Grüneis, C. Laubschat, D.V. Vyalyikh, *Nano Lett.* 14 (2014) 4982.
- [52] W. Zhao, O. Höfert, G. Gotterbarm, J. Zhu, C. Papp, H.-P. Steinrück, *J. Phys. Chem. C* 116 (2012) 5062.
- [53] U. Bangert, W. Pierce, D.M. Kepaptsoglou, Q. Ramasse, R. Zan, M.H. Gass, J.A. Van den Berg, C.B. Boothroyd, J. Amani, H. Hofsäss, *Nano Lett.* 13 (2013) 4902.
- [54] P. Willke, J.A. Amani, A. Sinterhau, S. Thakur, T. Kottz, T. Druga, S. Weikert, K. Maiti, H. Hofsäss, M. Wenderoth, *Nano Lett.* 15 (2015) 5110.
- [55] T. Kondo, D. Guo, T. Shikano, T. Suzuki, M. Sakurai, S. Okada, J. Nakamura, *Sci. Rep.* 5 (2015) 16412.
- [56] M. Telychko, P. Mutombo, M. Ondráček, P. Hapala, F.C. Bocquet, J. Kolorenč, M. Vondrávek, P. Jelínek, M. Švec, *ACS Nano* 8 (2014) 7318.
- [57] A. Martín-Recio, C. Romero-Muñiz, P. Pou, R. Pérez, J.M. Gómez-Rodríguez, *Nanoscale* 8 (2016) 17686.
- [58] O. Custance, S. Brochard, I. Brihuega, E. Artacho, J.M. Soler, A.M. Baró, J.M. Gómez-Rodríguez, *Phys. Rev. B* 67 (2003), 235410.
- [59] A.J. Martínez-Galera, J.M. Gómez-Rodríguez, *J. Phys. Chem. C* 115 (2011) 11089.
- [60] I. Horcas, R. Fernández, J.M. Gómez-Rodríguez, J. Colchero, J. Gómez-Herrero, A.M. Baró, *Rev. Sci. Instrum.* 78 (2007) 013705.
- [61] G. Kresse, J. Furthmüller, *Phys. Rev. B* 54 (1996) 11169.
- [62] P.E. Blöchl, *Phys. Rev. B* 50 (1994) 17953.
- [63] G. Kresse, D. Joubert, *Phys. Rev. B* 59 (1999) 1758.
- [64] J.P. Perdew, K. Burke, M. Ernzerhof, *Phys. Rev. Lett.* 77 (1996) 3865.
- [65] S. Grimme, *J. Comput. Chem.* 27 (2006) 1787–1799.
- [66] C. Romero-Muñiz, A. Martín-Recio, P. Pou, J.M. Gómez-Rodríguez, R. Pérez, *Carbon* 101 (2016) 129.
- [67] H.J. Monkhorst, J.D. Pack, *Phys. Rev. B* 13 (1976) 5188.
- [68] J. Tersoff, D.R. Hamann, *Phys. Rev. Lett.* 50 (1983) 1998.
- [69] J. Tersoff, D.R. Hamann, *Phys. Rev. B* 31 (1985) 805.
- [70] L. Zhao, R. He, K.T. Rim, T. Schiros, K.S. Kim, H. Zhou, C. Gutiérrez, S.P. Chockalingam, C.J. Arguello, L. Pálková, D. Nordlund, M.S. Hybertsen, D.R. Reichman, T.F. Heinz, P. Kim, A. Pinczuk, G.W. Flynn, A.N. Paspupathy, *Science* 333 (2011) 999.
- [71] T. Kondo, S. Casolo, T. Suzuki, T. Shikano, M. Sakurai, Y. Harada, M. Saito, M. Oshima, M.I. Trioni, G.F. Tantardini, J. Nakamura, *Phys. Rev. B* 86 (2012), 035436.
- [72] B. Zheng, P. Hermet, L. Henrard, *ACS Nano* 4 (2010) 4165.
- [73] A. Zabet-Khosousi, L. Zhao, L. Pálková, M.S. Hybertsen, D.R. Reichman, A.N. Paspupathy, G.W. Flynn, *J. Am. Chem. Soc.* 136 (2014) 1391.
- [74] P. Sutter, J.T. Sadowski, E.A. Sutter, *J. Am. Chem. Soc.* 132 (2010) 8175.
- [75] E.N. Voloshina, N. Berdunov, Y.S. Dedkov, *Sci. Rep.* 6 (2016) 20285.
- [76] R. Larciprete, S. Ulstrup, P. Lacovig, M. Dalmiglio, M. Bianchi, F. Mazzola, L. Hornekær, F. Orlando, A. Baraldi, P. Hofmann, S. Lizzit, *ACS Nano* 6 (2012) 9551.
- [77] N. Ligato, A. Cupolillo, L.S. Caputi, *Thin Solid Films* 543 (2013) 59.
- [78] N. Ligato, L.S. Caputi, A. Cupolillo, *Carbon* 100 (2016) 258.